PNAS RESEARCH ARTICLE | APPLIED PHYSICAL SCIENCES
APPLIED BIOLOGICAL SCIENCES

Silk-protein-based gradient hydrogels with multimode reprogrammable shape changes for biointegrated devices

Yushu Wang[a,b], Luhe Li[a], Yue-E. Ji[a], Tao Wang[a], Yinghao Fu[a], Xinxin Li[b], Guicai Li[c], Tiantian Zheng[c], Linliang Wu[c], Qi Han[c], Ye Zhang[a], Yu Wang[a,1], David L. Kaplan[b,1], and Yanqing Lu[a,1]

Edited by David Weitz, Harvard University, Cambridge, MA; received April 9, 2023; accepted July 11, 2023

Biocompatible and morphable hydrogels capable of multimode reprogrammable, and adaptive shape changes are potentially useful for diverse biomedical applications. However, existing morphable systems often rely on complicated structural designs involving cumbersome and energy-intensive fabrication processes. Here, we report a simple electric-field-activated protein network migration strategy to reversibly program silk-protein hydrogels with controllable and reprogrammable complex shape transformations. The application of a low electric field enables the convergence of net negatively charged protein cross-linking networks toward the anode (isoelectric point plane) due to the pH gradient generated in the process, facilitating the formation of a gradient network structure and systems suitable for three-dimensional shape change. These tunable protein networks can be reprogrammed or permanently fixed by control of the polymorphic transitions. We show that these morphing hydrogels are capable of conformally interfacing with biological tissues by programming the shape changes and a bimorph structure consisting of aligned carbon nanotube multilayers and the silk hydrogels was assembled to illustrate utility as an implantable bioelectronic device for localized low-voltage electrical stimulation of the sciatic nerve in a rabbit.

silk | electrical | hydrogel | shape-change | interface

Living creatures, ranging from plants to marine invertebrates, demonstrate exquisite body structures and designs that enable them to execute complex, adaptive shape transformations for morphogenesis, growth, or adapting to surrounding environments (1–3). These sophisticated biological morphing systems provide inspiration for the development of materials that can perform geometric shape deformations in response to external stimuli, driving a generation of soft and smart actuators for a variety of application scenarios, including soft robotics, flexible electronics, heliotracking systems, and biological interfaces (4–7). Existing artificial actuation systems use diverse stimulus-responsive materials, such as liquid crystal elastomers (8–10), hydrogels (11–14), silicone elastomers (15), and shape-memory polymers (16, 17), to achieve targeted deformation, such as bending, folding, twisting, and buckling. Stimulus-responsive hydrogels have emerged as promising active materials for the development of smart actuation systems to reproduce the multidegree-of-freedom shape transformation behaviors of living organisms due to their intrinsic biological-tissue-like softness, aqueous nature, and flexibility in functionalization (18–20). In particular, the compliance, adaptivity, and mechanical properties of hydrogel actuators make them attractive for various biomedical scenarios through reliable interfaces with the living tissues (21, 22).

With these advantages of hydrogel actuators, extensive efforts have been devoted to inventing advanced techniques to transform two-dimensional (2D) hydrogels into three-dimensional (3D) shapes. A prevalent strategy relies on encoding spatial heterogeneity (e.g., cross-link density, composition, filler distribution/orientation) by leveraging fabrication methods such as photolithography, molding, 3D/4D printing, and electrodeposition, to support responses to temperature, magnetic fields, light, electricity, and chemicals (11–13, 23–30). In addition, encapsulating active components into homogeneous hydrogel matrices provides another straightforward approach for the fabrication of shape transformable actuators (31–33). The advances in implementing controllable, reversibly programmable, and multimodal morphing functions with these strategies facilitates applications of shape-morphing hydrogels in different biomedical realms, including soft medical robotics, tissue repair, cell manipulation, organ-on-a-chip, and drug delivery (29, 34–36). Despite significant progress toward these goals, existing hydrogel systems mostly built from synthetic polymers usually involve a complicated molecular organization requiring cumbersome and energy-intensive synthetic processes. In addition, the growing development of hydrogel-based actuating systems in biomedical engineering requires stimulus-responsive materials that are more compatible with biological tissues. Therefore, the development of

Significance

Biocompatible hydrogel actuation systems have attracted attention in various biomedical scenarios due to their compliance, adaptivity, and mechanical properties. The present work demonstrates the use of silk protein to generate stimulus-responsive hydrogel systems that can morph reversibly and controllably. This was achieved by an electric-field-driven protein chain migration strategy that enabled the formation of gradient network structures by exploiting the net negative charge of silk fibroin protein chains. The capacity to dynamically manipulate protein network architecture in multiple ways allows for multimode, reprogrammable, and complex material shape deformations, making these gradient hydrogels amendable to various functional devices. The confluence of a versatile protein format and programmable shape transformation also offers directions for interfaces between soft robotic technologies and biological tissues.

The authors declare no competing interest.

This article is a PNAS Direct Submission.

[1]To whom correspondence may be addressed. Email: yuwang87@nju.edu.cn, david.kaplan@tufts.edu, or yqlu@nju.edu.cn.

This article contains supporting information online at https://www.pnas.org/lookup/suppl/doi:10.1073/pnas.2305704120/-/DCSupplemental.

Published August 7, 2023.

physiologically compliant actuators with biocompatible building blocks, simple structure designs, multimodal and reprogrammable shape-morphing, adaptive deformations, and multiple functions through simple fabrication processes is desired.

In this context, shape-morphing hydrogels using naturally derived biopolymers as the primary building blocks provide an appealing platform for interfaces between soft robotic technologies and biological tissues. Silk fibroin (SF) extracted from native *Bombyx mori* (*B. mori*) silkworm fibers (Scheme 1*A*) is particularly relevant here because of its convergence of biocompatibility, aqueous processability, stimulus-responsiveness, tailorable and robust mechanical properties, multiscale and multimode manufacturing, polymorphic structures, and ease of functionalization (37–41). Here, we describe the facile construction of silk-protein-based electric-field-driven gradient hydrogels that transform from 2D hydrogels into multimodal, reprogrammable, and complex 3D configurations (Scheme 1*B*). We show that a variety of gradient structures can be written into the hydrogels by deploying electric-field distributions of sol–gel transitions, which can thereby induce controllable migration of silk-protein networks, enabling the arbitrary construction of distinct 3D configurations. We demonstrate that the reversible migration of these protein networks allows the reconstruction of gradient structures and, thus, the reprogramming of 3D deformations, all in one hydrogel. Further, while these systems are reversible, if desired, these 3D shapes can be permanently fixed by modulating the protein conformation by a simple ethyl alcohol (EtOH) treatment. Finally, we demonstrate that these protein-based shape-morphing systems can be used as biointegrated devices for conformal interfaces with biological tissues (Scheme 1*C*).

Results

Shape-Morphable Gradient Hydrogels. The formation of SF hydrogels with gradient network structures (SF-G-gel) is based on an electric-field-induced protein network migration strategy (Fig. 1*A*). By injecting a solution containing SF, horseradish peroxidase (HRP), and hydrogen peroxide (H_2O_2) between two transparent electrodes [ITO (indium-tin oxide) glass] with the aid of a polydimethylsiloxane (PDMS) mold, a transparent and homogeneous hydrogel (SF-H-gel) forms via the HRP-catalyzed free radical cross-linking of the tyrosine residues on the SF in the presence of H_2O_2 (42). Subsequently, a stable electric field (E = 1 V mm^{-1}) was applied to induce the migration of the overall negatively charged protein cross-linking networks toward the anode to form a gradient hydrogel at room temperature. The shape morphing hydrogel was obtained after removing the gel from the electrodes.

The generation of gradient network structure driven by the electric field is the key to preparing morphing hydrogels and is based on isoelectric focusing (43, 44). The application of an external electric field causes electrolysis of the water within the hydrogel around the electrodes, generating H^+ and OH^- at the anode and cathode, respectively. The continuous generation of ions around the electrodes results in the formation of a pH gradient between the two electrodes; the hydrogel near the anode becomes acidic with a pH of ~4, whereas the hydrogel near the cathode becomes basic with a pH of ~10, as indicated by the pH indicator strips (*SI Appendix*, Fig. S1). Silk molecules are negatively charged in a neutral aqueous environment with an isoelectric point (pI) of 4.2 due to the higher content of acidic charged groups in the amorphous domains in comparison to basic charged groups (Fig. 1 *B* and *C*) (45, 46). Therefore, upon the induction of the electric field, the charged protein cross-linked networks migrated toward the anode (Fig. 1*D*), where the net charge approached zero (i.e., pI), since the pH value in the vicinity of the anode was close to the pI of silk. The accumulation of protein molecules near the anode led to the formation of a gradient of cross-link density within the hydrogel (Fig. 1*D*). This gradient network structure generated unbalanced forces between the two sides of the hydrogel, the main driving force for shape transformations. The presence of a higher protein cross-link density closer to the anode side of the

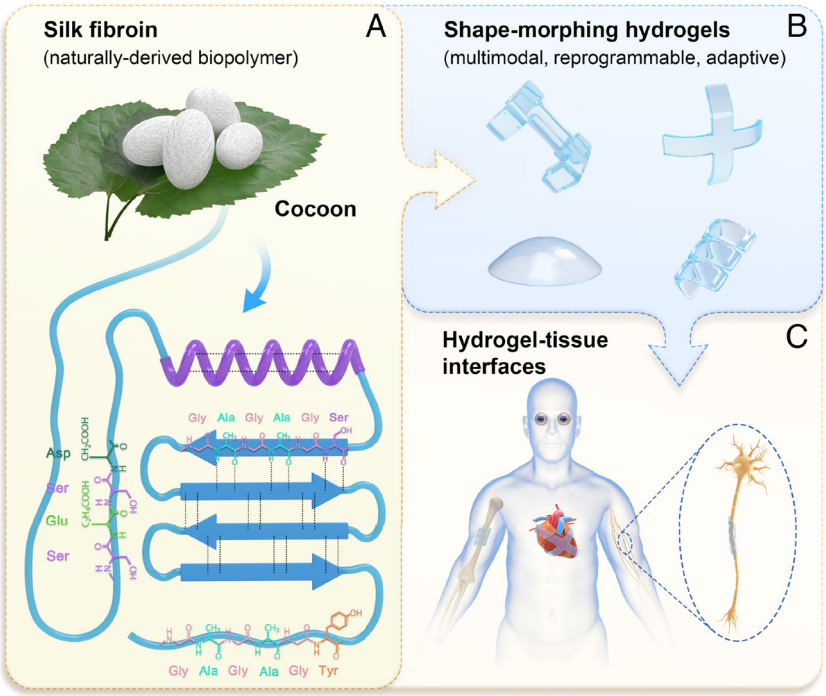

Scheme 1. Shape-morphing hydrogels based on SF for biointegrated devices. (*A*) *B. mori* silkworm cocoons derived SF and its molecular chain showing the primary chemical composition and secondary structures (random coil, β-sheet, helix). (*B*) Shape-morphing hydrogels with multimodal, reprogrammable, and adaptive 3D deformation behavior. (*C*) Interfaces between morphing hydrogels and biological tissues.

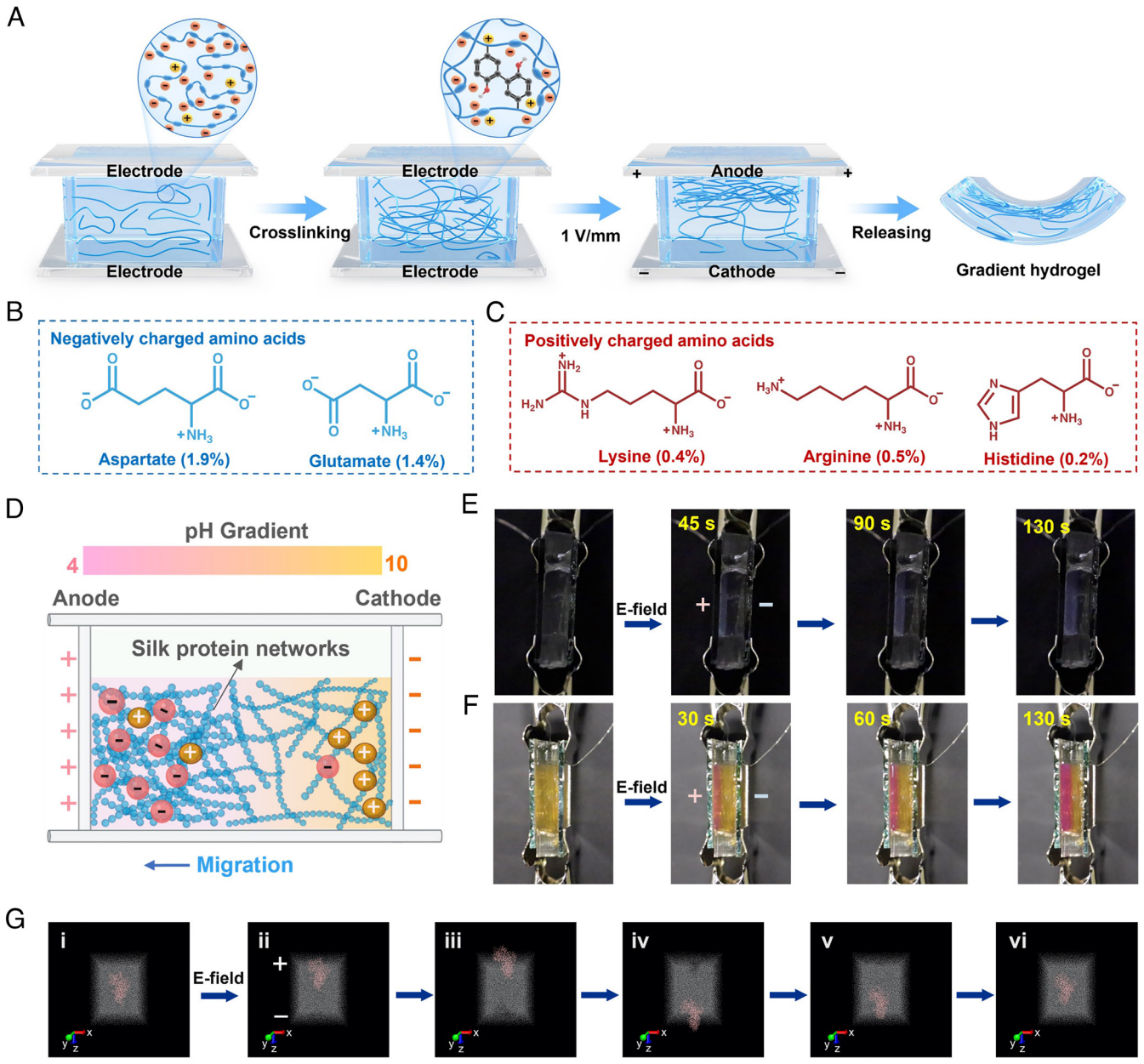

Fig. 1. Formation and mechanism of the silk-based shape-morphable gradient hydrogels. (*A*) Schematic of fabrication of shape-morphing hydrogels with a gradient network structure. Under an electric field, the chemically cross-linked protein chains migrate toward the anode, resulting in the formation of gradient networks. Shape-morphing hydrogels are achieved after releasing the hydrogel from the electrodes. (*B* and *C*) The negatively (*B*) and positively (*C*) charged amino acids contained within silk protein and their corresponding content. (*D*) Schematic of silk-protein network migration induced by an electric field in the presence of a pH gradient. (*E*) Photographs showing the gradual accumulation of silk-protein networks near the anode with an electric field. The opaque area indicates converged protein networks. (*F*) The corresponding evolution of pH within the hydrogel, indicated by doping the silk hydrogel with methyl red indicator dye. (*G*) Representative snapshots during molecular dynamics simulation of silk-protein migration within the applied electrical field. (*i*) Initial silk protein structure for the simulation. (*ii-vi*) Movement trajectory of the silk protein under the electric field.

gel enabled the hydrogel to store more strain energy in this region, thus, yielding bending deformation toward the anode after releasing the strain energy.

The dynamic migration of the protein networks was observed in situ. As shown in Fig. 1*E*, the opaque convergent protein networks appear in front of the anode within a few seconds and then gradually extend toward the cathode with constant electric field stimulation (Movie S1). The migration rate is positively correlated with the applied electric field strength. Generally, a gradient structure with a thickness of 2.5 mm (in a 5-mm-thick hydrogel) would be generated after applying electric field of 1 V/mm for 130 s. The evolution of the pH gradient and formation of the gradient hydrogel was analyzed by mixing the hydrogel with methyl red, a pH indicator dye that appears red when pH is lower than 4.4 and yellow when pH is higher than 6.2. As observed from Fig. 1*F* and Movie S2, the color changes from yellow to red near the anode after applying the electric field for a few seconds, and the red color gradually penetrates the hydrogel with time, demonstrating the generation of H^+ and its migration from anode toward the cathode.

To further elucidate the mechanism of gradient formation, molecular dynamics (MD) simulations of protein chain motion under electric field stimulation were carried out (Fig. 1*G*). A MD approach for ab initio structure prediction of silk proteins was utilized to obtain stable structures (*SI Appendix*, Fig. S2*A*). Then, the structure of the silk protein was further optimized under explicit solvent conditions, and the resulting final structure was

taken as the starting structure for the simulation under electric field conditions. The simulated trajectory indicates that the silk-protein motion consistently follows the opposite direction of the applied electric field of 5 mV/Å, and the direction of the silk-protein motion shifts upon alteration of the electric field direction (*SI Appendix,* Fig. S2*B*). In addition, the rmsd results showed no drastic fluctuations of signals with electric fields of different strengths, indicating the stability of protein molecular structure upon the electric field stimulation (*SI Appendix,* Fig. S2*C*). Furthermore, the silk-protein motion trajectory results were further analyzed by quantitively calculating migration rate. The result revealed that migration rate demonstrates an increase with higher electric field strength, while the migration direction undergoes a shift corresponding to changes in the direction of the electric field (*SI Appendix,* Fig. S2*D*). The combination of reversible electric field responsiveness, a tunable cross-linking network, and robust mechanical performance of the hydrogels enables the capacity to reprogram the gradient structure to achieve the morphing behavior, and the final 3D configurations.

Characterization of Gradient Hydrogels. To verify the formation of protein network gradients and analyze the distribution, the internal morphology of SF-G-gels was investigated using freeze-drying methods. Cross-section scanning electron microscopy (SEM) images of the freeze-dried SF-G-gel exhibited a decrease in pore size from the cathode to the anode (Fig. 2*A*), which indicates gradient network formation in the hydrogel under electric field. The convergence of protein networks leads to the higher cross-link density and the smaller pore size. Moreover, X-Ray 3D microscopy was implemented to characterize the 3D gradient distribution of the protein network structure within the SF-G-gels. Denser pore structures were observed near the anode than the cathode, consistent with the SEM results (Fig. 2*B*). From the transverse profiles (Fig. 2 *B*, *iii* and *iv*), the gradient was distributed throughout the hydrogel. It is worth noting that both the SEM and X-ray 3D microscopy images show the front of the aggregated protein networks (Fig. 2 *A*, *ii* and Fig. 2 *B*, *i*). Fourier-transform infrared spectroscopy (FTIR) measurements showed that the gradient hydrogel was still in the amorphous state, demonstrating no conformational change of the hydrogel in response to electric field treatment (Fig. 2*C*). The SF-G-gel exhibited a remarkable mechanical gradient; it is rigid at the anode and soft at the cathode. Rheology measurements revealed that the storage modulus (G′) values of all hydrogels were higher than their loss modulus (G″), indicating the formation of stable hydrogels (Fig. 2*D* and *SI Appendix,* Fig. S3). Frequency sweep results showed that G′ of SF-G-gel decreased from 13.5 kPa at the anode to 4.3 kPa at the cathode, while the SF-H-gel showed an intermediate value of 9.7 kPa (Fig. 2*D*), confirming the presence of mechanical gradient within the SF-G-gel. Additionally, the results obtained from frequency and time sweeps indicated that both G′ and G″ of the two hydrogels remained consistent within the frequency range of 10^{-1} to 10^{2} rad/s and a time duration of 600 s, which is crucial for ensuring stable and efficient actuation behaviors of the hydrogels.

The initial cross-link density of the SF-H-gel, which determines the migration dynamics of the protein chains, has a significant influence on the optical transmittance of the final gradient hydrogel. By varying the final concentration of H_2O_2 in the system, we can generate SF-H-gels with different cross-link densities. The higher the concentration of H_2O_2, the higher the cross-link density and, thus mechanical stiffness (*SI Appendix,* Fig. S4 *A, C,* and *D*). These SF-H-gels show similar optical transmittance, but after electric field stimulation, the transmittance decreased with the decrease in cross-link density (Fig. 2*E*). At low cross-link density, such as with a H_2O_2 concentration of 0.3 mM (i.e., 0.3 mM SF-H-gel), a large number of free protein chains migrate and accumulate near the anode [like the behavior of pure SF solution (46, 47)], resulting in the formation of SF-G-gels with lower transmittance than the corresponding SF-H-gels (Fig. 2*E*). However, with increased cross-link density, the migration process was gradually dominated by the cross-linked protein networks, which had little effect on the transmittance of the final gradient hydrogel. The use of patterned ITO as the anode provided a straightforward approach to reversibly visualize gradient formation of low cross-link density hydrogels, making the final devices potentially able to encode/decode patterns in deformations by switching the power on/off. As an example, and as shown in Fig. 2*F* a white butterfly pattern appeared after applying voltage, and becomes invisible again after turning the power supply off (Movie S4).

Self-Deformation for 3D Shape Change. While hydrogels with different cross-link densities form gradients under an electric field, we found that only those with high cross-link density (specifically, the 4 mM SF-H-gel among the examined SF-H-gels with different cross-link densities) and thus high mechanical strength (*SI Appendix,* Fig. S4*B*) stored sufficient strain energy to induce macroscale shape transformations. Therefore, all the hydrogels considered here are 4 mM SF-H-gel unless otherwise noted. To evaluate the role of the gradient distribution in shape transformation, the 3D self-deformation ability of SF-G-gels with different electric field stimulation times was quantitatively characterized. Hydrogel strips measuring 25 × 5 × 2 mm were first generated with the aid of PDMS molds. Fig. 3*A* plots the measured curvature for different durations of the applied electric field. After exposure to the electric field of 1 V/mm, the straight strip deformed into an arc shape and its curvature increased with increasing exposure time, consistent with the result of gradient evolution (Fig. 1*E* and Movie S1). In addition to simple bending deformation, circular discs could also be deformed into bowl-shaped configurations of different curvatures (Fig. 3*B*). It is worth noting that the hydrogel's displacement (or curvature) and actuation rate, which are two crucial parameters for assessing the performance of an actuator, are determined by several factors, including the hydrogel's thickness, cross-link density, and applied electric field strength/duration. Finding the careful balance and the optimal combination of these factors is crucial for achieving high-speed and large-deformation actuation, as well as the desired actuation capabilities.

The electric-field-dependent actuation enables the construction of complex 3D configurations by spatially encoding gradient distributions by switching directions of the electric field, patterning of the hydrogel, and/or patterning the electrodes. As shown in Fig. 3*C*, an 8-shaped SF-G-gel was demonstrated by applying two pairs of electrodes and switching the direction of the electric field. A cross-shaped geometry supported the formation of a bud-shaped hydrogel (Fig. 3*D*). Moreover, when the electric field was only applied in the middle part of a wheel-shaped hydrogel, the whole wheel arched up to generate a helmet-shape (Fig. 3*E*). More complex shape transformations can be achieved by inducing out-of-plane deformations through the Kirigami technique (48). To demonstrate this outcome, a four-arm pinwheel pattern was generated in a hydrogel using a laser cutting technique. After electric field stimulation, the structure buckles up with the twisting of the four arms (Fig. 3*F*). Another example is an upward bent concentric "petal" array with spatial arrangement of the curvature (Fig. 3*G*). By applying three toroidal electric fields of different durations to the structure, bending deformation gradually increased the

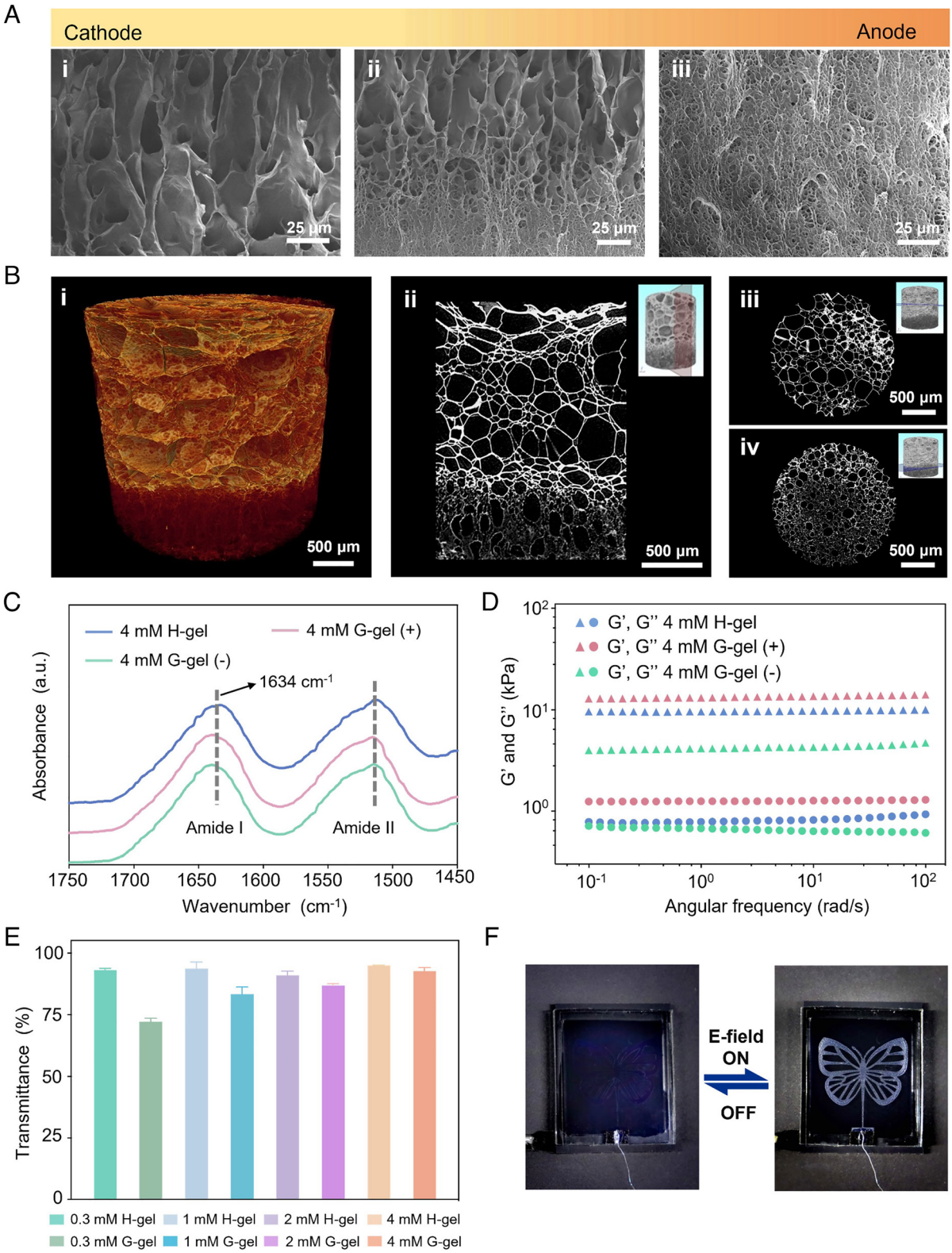

Fig. 2. Morphology, structure, and properties of gradient hydrogels. (*A*) Cross-section SEM images of the SF-G-gel, showing decreasing pore size from the cathode (*i*) to the anode (*iii*). (*B*) 3D-X-ray scan of SF-G-gel: (*i*) 3D reconstruction of the SF-G-gel, (*ii–iv*) Extracted 2D cross-section images with cutting plane shown in the corresponding inset. (*C* and *D*) FTIR (*C*) and rheology (*D*) analyses of the SF-G-gel near the anode (+) and the cathode (−), and the corresponding SF-H-gel. (*E*) Transmittance values of the SF-H-gels and the resulting SF-G-gels with various cross-link densities. (*F*) Photographs showing the reversible display of the butterfly pattern induced by an electric field. The device consists of a 0.3 mM SF-H-gel sandwiched between a normal ITO glass and a butterfly patterned ITO glass.

curvatures from the outermost to the innermost ring due to the differences in the gradients. To gain a better understanding of the morphing behavior of the hydrogel, we conducted finite element analysis (FEA) to verify the various deformation modes exhibited by the hydrogels under electric field stimulation. The calibrated finite element model successfully reproduces the final transformations of the hydrogels, as observed in the experimental results. This demonstrates the accuracy and reliability of the finite element model

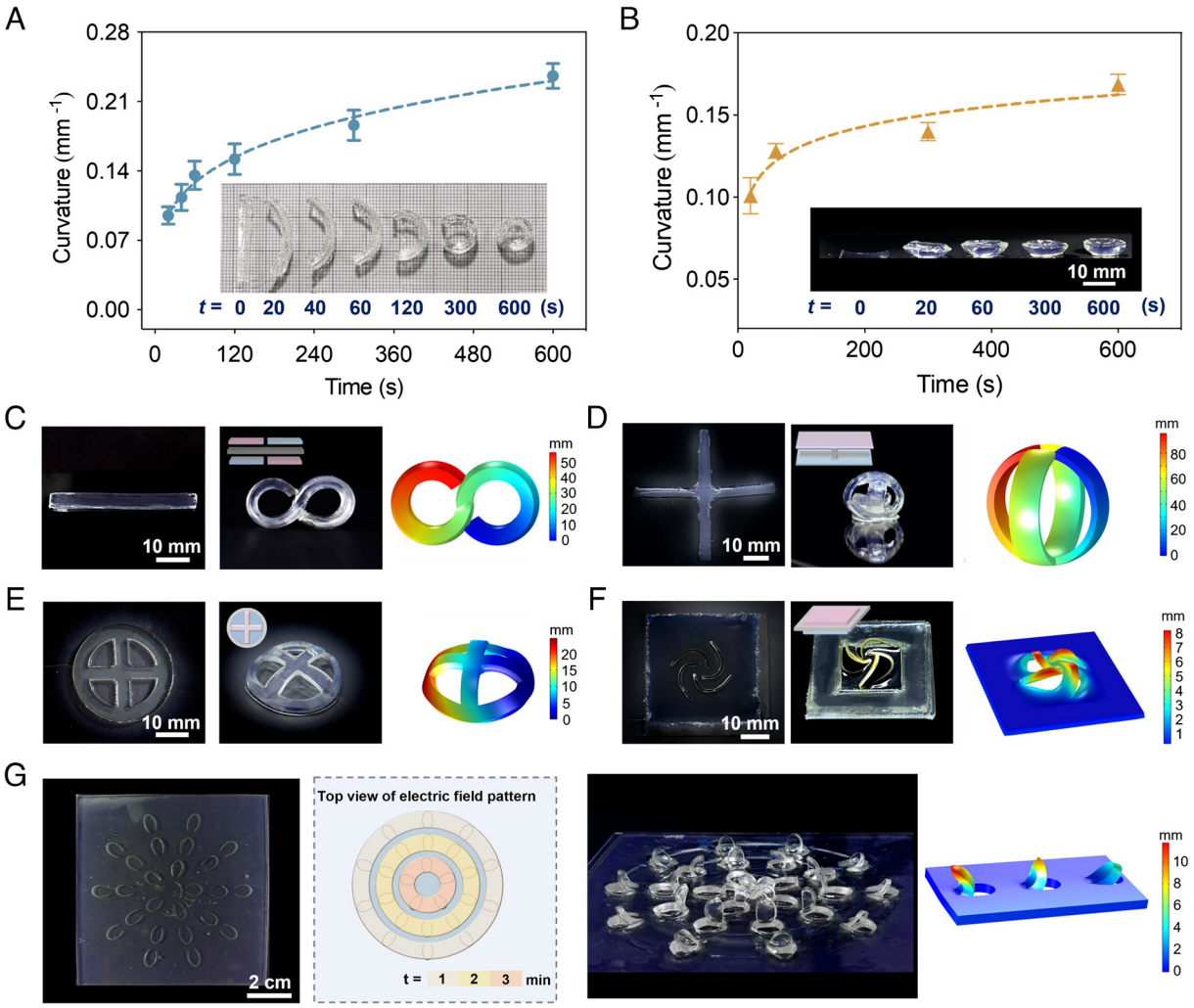

Fig. 3. Controllable and programmable shape-morphing. (*A* and *B*) Dependence of curvature of a SF-G-gel strip (*A*) or circular disc (*B*) on the electric field induction time. Insets are the corresponding photographs of SF-G-gels with different curvatures. (*C*–*F*) Photographs of the designed 2D structures (*Left*) and the corresponding 3D configurations after stimulation in the electric field (*Middle*). (*Right*) Predicted shape transformation by FEA. Insets indicate electric field application modes. The pink color represents the anode, the blue color the cathode. (*G*) (*Left* to *Right*) Photograph of a 2D concentric "petal" pattern, schematic illustration of the electric field pattern, photograph showing the incremental bending deformation from the outermost to the innermost ring, and the predicted 3D deformation of a unit.

in capturing and replicating the actual behavior of the hydrogels during the morphing process. This finding further demonstrates that on-demand 3D architectures can be successfully achieved by manipulating the distribution of gradient structure and the original geometry of hydrogel.

Conformation-Mediated Reprogrammable Shape-Morphing and Permanent Shape Fixation. Although programming the gradient distribution effectively transforms the 2D structures into different 3D configurations, reversible and tunable shape changing is feasible in the hydrogel. The aggregation of protein networks near the anode stimulated by the applied electrical field does not elicit changes in the protein conformation, as already noted. This characteristic implies the absence of new physical anchor points forming within the protein networks. Consequently, the protein chains are capable of unrestricted and reversible movement in response to specific external stimuli. Given that the gradient structures are in a nonsteady state due to the presence of unbalanced forces, they exhibit a tendency to progress toward the initial uniform network distribution through the redistribution of the gradient protein networks when keeping the gradient hydrogels in a wetted state (Fig. 4*A*). By incubating the deformed hydrogel in water, the gradient structure can be dissipated, thus resetting the hydrogel to the shape to the original flat state that can be reprogrammed again by reapplying electric field. In addition, switching electric field directions provides a strategy for in situ reprogramming of the gradient structure. As shown in Fig. 4*B*, a low electric field induced the accumulation of protein networks near the anode, upon alternating the field direction, the aggregated protein chains dissipated and now aggregated at the opposite electrode. This reprogrammable gradient distribution can be encoded in a single hydrogel to enable tunable deformation and switchable 3D configurations. As a proof-of-concept demonstration, an H-shaped structure was constructed to respond to different electric field distributions (Fig. 4*C*). When the electrodes fully covered the upper and lower surfaces of the SF-H-gel, the uniformly distributed gradients caused the curling of the whole hydrogel into a closed structure. The deformed SF-G-gel recovered the flat shape after equilibrating in water to erase the gradient structure. The recovered H-shaped geometry was reprogrammed by placing two pairs of symmetrical electrodes on the four arms to induce deformation only for the arms. The encoded hydrogel morphed into a table-like shape. Following further recovery of the SF-G-gel to its original shape again, an inverse Z-shaped configuration was achieved by alternating the electric field direction of two

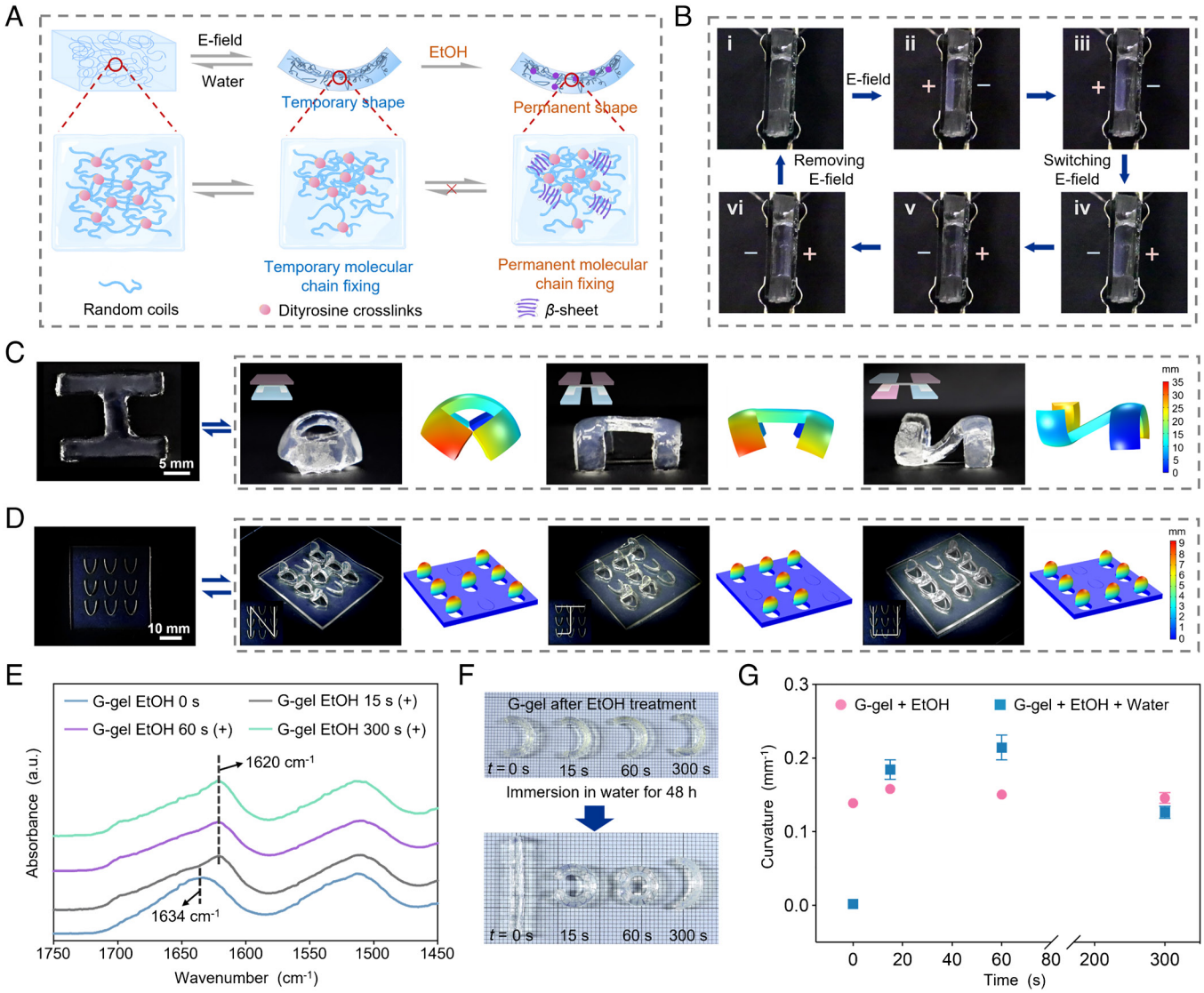

Fig. 4. Water-induced reversible shape change and EtOH-triggered permanent shape fixation. (*A*) Schematic of reversible temporary shape morphing induced by water immersion and permanent shape fixation induced by EtOH exposure. (*B*) Photographs showing the reversal of the gradient structure through switching the direction of the electric field. The opaque area indicates aggregation of protein networks near the anode. (*C* and *D*) Reprogrammable deformations of an H-shaped hydrogel (*C*) and a Kirigami pattern (*D*) based on rewritable gradient structures. The reversible transformation between 3D and 2D structures was obtained by applying electric field and water, respectively. Predicted shape transformation by FEA is also shown. *Insets* in *C* indicate the electric field application modes. *Insets* in *D* show the patterns generated by controlled shape-morphing of the petal-shaped units. (*E*) FTIR spectra of SF-G-gels near the anode after EtOH treatment. The spectrum shows a peak shift from 1,634 cm^{-1} to 1,620 cm^{-1} after EtOH exposure, indicating the formation of β-sheet conformation (thus, aqueous insolubility via locking in the structure). (*F*) Photographs showing the influence of EtOH treatment on the recovery of 3D configurations induced by immersion in water. (*G*) Calculated curvature of gradient hydrogels before and after soaking in water as a function of EtOH treatment time.

pairs of symmetrical electrodes placed on the four arms. We also demonstrated reprogrammable Kirigami patterns by generating an array of petal-shaped geometries. As shown in Fig. 4*D*, the letters of "N", "J", and "U" can be successively displayed after sequentially encoding and erasing the gradient structures. In addition, and as before, FEA confirmed the experimental results, indicating the reliability of the reprogramming process.

In contrast, the ability to anchor the molecular networks of SF-G-gel by inducing the polymorphic transition of silk protein allows the permanent fixation of the gradient structure and, thus, the 3D shape (Fig. 4*A*). This can be achieved through, for example, EtOH exposure. FTIR results confirm the conformational transition (from random coil to β-sheet) of the gradient hydrogel induced by EtOH (Fig. 4*E* and *SI Appendix*, Fig. S5). After the exposure to EtOH, the formation of new physical anchor points consisting of β-sheet crystals resulted in the morphing hydrogel retaining its configuration without recovery, even after being immersed in water for more than 48 h. This was in contrast to the hydrogel without EtOH treatment (Fig. 4*F*). The slightly different curvatures of the deformed hydrogels induced by immersion in water can be ascribed to the swelling mismatch between the regions near the anode and cathode (Fig. 4*G*).

Biointegrated Devices. The capacity to direct the morphing process to construct distinct 3D configurations, together with the biocompatibility, mechanical properties, and ease of functionalization, make these SF-G-gels potentially applicable for biologically matched functional interfaces. To demonstrate this potential, the interfacial attachment between the morphing hydrogels and tissues with different 3D geometries, hardness, and textures was evaluated (Fig. 5 *A*–*C*). The SF-G-gels programmed into distinct configurations were capable of tightly attaching to the surfaces of a curved resin eyeball, rabbit heart,

and rabbit femur in both air and water environments without any additional fixation requirements. In comparison, the SF-H-gels do not make conformal contact with the organs to form good hydrogel–tissue interfaces, especially in the water environment. The same SF-G-gel with reprogrammable deformation displayed self-adaptation to different organs (*SI Appendix*, Fig. S6). These findings demonstrate that the formation of morphing with 3D configuration matching the topological morphology of the tissue surface significantly contributes to the establishment of a tight interfacial attachment between the hydrogel and the tissue. Notably, the silk gradient hydrogels stand out as adhesive-free, highly conformable, and easily detachable platforms, rendering them significantly distinct from the interfacial adhesive hydrogels typically employed in biointegrated devices (49, 50), which heavily depend on specific bonding or sticking to tissues. Besides

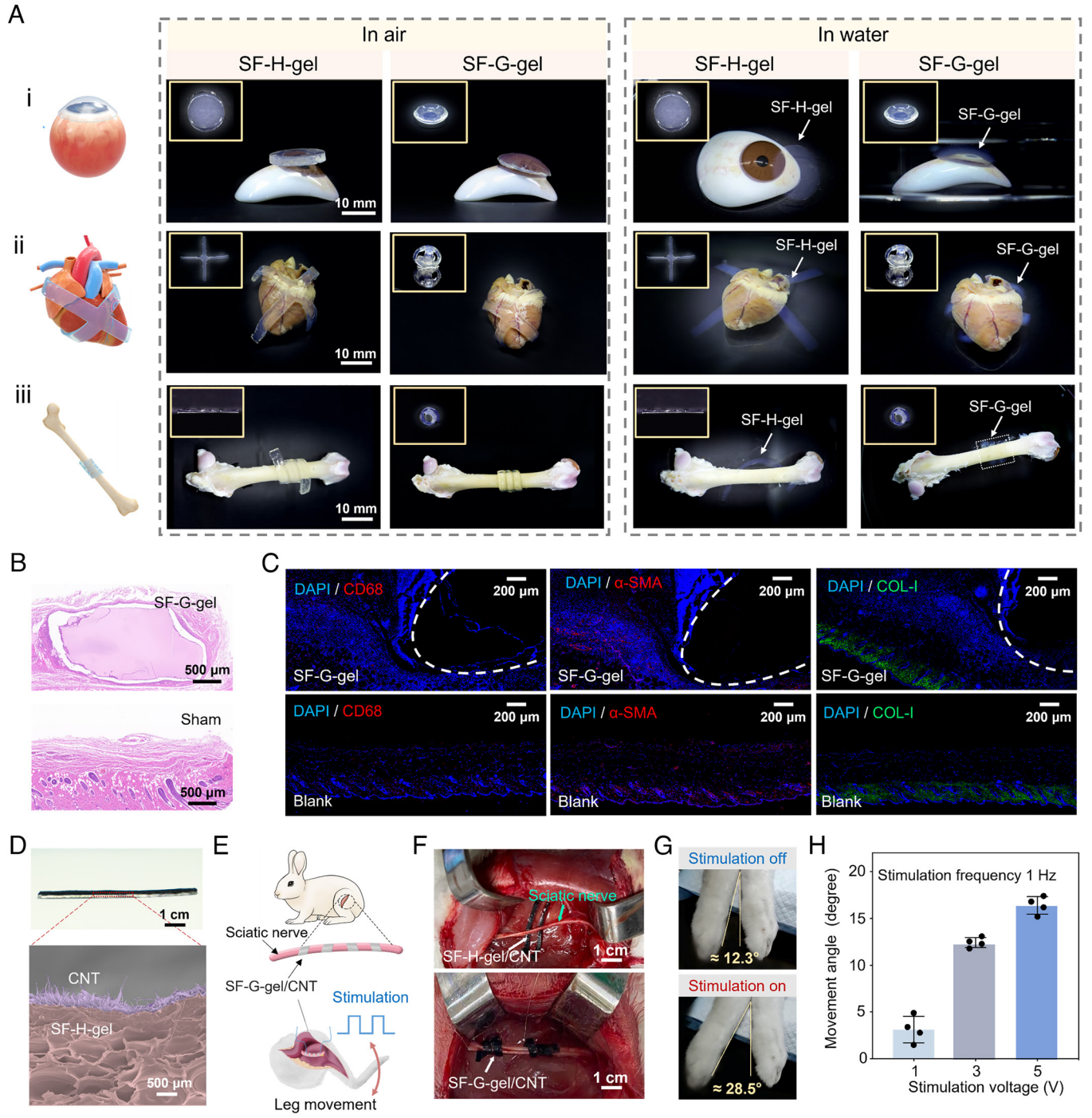

Fig. 5. Interface stability and biocompatibility of the morphing hydrogel and its application for biointegrated devices. (*A*, *Left*) Schematics showing the conformal contact between SF-G-gels and organs. (*Right*) Photographs of SF-H-gels of different geometries and corresponding SF-G-gels interfaced with organs in air and water. (*i*) prosthesis eyeball, (*ii*) rabbit heart, (*iii*) rabbit femur. (*B* and *C*) Representative histology images stained with H&E (*B*) and immunostaining (*C*) for tissue sections of skin, with and without SF-G-gels, after subcutaneous implantation in mice for 14 d. Cell nuclei were stained with DAPI in blue. Red fluorescence corresponds to the expression of CD68 and α-SMA, green fluorescence corresponds to the expression of COL-I. The areas circled by white dashes indicate the implanted hydrogel. (*D*) Photograph of a SF-H-gel/CNT electrode and enlarged cross-sectional SEM image showing the compact interface between CNT and SF-H-gel. (*E*) Schematic of the rabbit sciatic nerve stimulation setup. (*F*) Photographs showing the attachment of a pair of SF-H-gel/CNT electrodes (*Top*) and a pair of SF-G-gel/CNT electrodes (*Bottom*) on a sciatic nerve. (*G*) Photographs showing the motion of the rabbit leg in response to electrical stimulation via the morphing bioelectrodes. (*H*) Calculated movement angle of the rabbit leg under different stimulation voltages.

the conformal interfacial contact, biocompatibility of the SF-G-gel is key, thus, in vitro cytotoxicity and in vivo biocompatibility were studied. Cytotoxicity was analyzed by seeding bone marrow mesenchymal stem cells (BMSCs) on SF-G-gels and quantitatively calculating optical density at 450 nm to indicate cell density (*SI Appendix,* Fig. S7). The cells cocultured with the SF-G-gels showed similar values to the control (pristine culture medium) after 24-h culture, demonstrating the cytocompatibility of the SF-G-gels. Moreover, the in vivo biocompatibility of the SF-G-gel was assessed based on dorsal subcutaneous implantations in a mouse model for 14 d. Histological staining was performed to evaluate local inflammatory responses, which suggested that the SF-G-gel showed minimal inflammatory responses (Fig. 5*B*). To visualize and quantitatively characterize the immune responses of the SF-G-gels, biomarkers associated with inflammation induced foreign body responses and tissue regeneration, including CD68 for macrophages, α-smooth muscle actin (α-SMA) for fibroblasts, and collagen type I (COL-I) for collagen were also investigated through immunofluorescence staining. No significant expression of these biomarkers was observed in subcutaneous tissues implanted with the SF-G-gels, as indicated by immunofluorescence images (Fig. 5*C*) and quantitative analysis (*SI Appendix,* Fig. S8), suggesting that the SF-G-gel were biocompatible. The in vitro degradation results demonstrated that the SF-G-gels exhibited comparable degradation rates to the SF-H-gels (*SI Appendix,* Fig. S9). Moreover, both hydrogels exhibited accelerated degradation profiles as the concentrations of the protease solutions increased, indicating their ability to undergo controlled degradation in response to enzymatic activity.

To demonstrate the practical biomedical implications of the gradient hydrogels, we constructed a flexible bioelectronic device matched to tissue mechanics and illustrated its utility as conformal bioelectrodes for sciatic neural stimulation based on a rabbit model. The bioelectronic system is a bimorph structure consisting of aligned carbon nanotube (CNT) multilayers and the silk hydrogel (Fig. 5*D*). The CNT sheets with high conductivity, flexibility, and integrity act both as the anode to induce the formation of morphing bilayer (*SI Appendix,* Fig. S10*A*) and as the electrodes to electrically stimulate the sciatic nerve. The introduction of the CNT layer did not compromise the deformation performance of the gradient hydrogel because of its flexible features as well as the stable interface between the CNT layer and the hydrogel (Fig. 5*D*), thereby supporting a compact physical interface with the nerve. The morphing bioelectronic device exhibited low impedance (<100 ohms) at physiologically relevant frequencies of 10^2 to 10^5 Hz (*SI Appendix,* Fig. S10*B*), and no significant impedance changes for the morphing SF-G-gel were observed after soaking in PBS solution for 24 h (*SI Appendix,* Fig. S10*C*), indicating stable electrical conductivity of the bilayer SF-G-gel/CNT system. The charge injection capability (CIC) value reached ~150 μC cm^{-2} (*SI Appendix,* Fig. S11), allowing efficient electrical communication between the bioelectronic device and the underlying nerve during electric stimulation (49, 50). In addition, the generation of stable and efficient electrical communication of the deformed bioelectronic device was also demonstrated by its ability to confer light-emitting diode stable signal output and higher brightness in comparison with the flat device (*SI Appendix,* Fig. S12). To further evaluate in vivo functionality, a pair of morphing electrodes was implanted on the sciatic nerve of a rabbit to investigate electrical stimulation efficacy by monitoring the movement of the leg, as schematically shown in Fig. 5*E*. The electrodes without shape-morphing showed limited contact with the sciatic nerve and did not result in movement of the leg (Fig. 5 *F*, *Top*). In contrast, the morphing electrodes tightly wrapped the sciatic nerve and maintained conformal integration during stimulation (Fig. 5 *F*, *Bottom*). Under electrical stimulation (1 to 5 V at 1 Hz), stable and periodic movements of the leg driven by the muscle contraction caused by the electric stimulation of the sciatic nerve were observed (Fig. 5*G* and Movie S5). The degree of movement increased with elevated voltage (Fig. 5*H*), as expected. These findings demonstrate that morphing bioelectronic devices were more effective at transmitting electric signals to nerve tissue than the control flat devices.

Discussion

Silk-based, transparent, robust, and shape-morphable gradient hydrogels were prepared and demonstrated to provide reprogrammable control of network structures and 3D configurations. The capacity to arbitrarily encode the gradient structures by engineering electrical field distributions enables programming of shape-morphing into various complex 3D configurations. This electric-field-driven programming strategy allows controlled gradient distributions at the microscale, providing opportunities for microscaled 3D shape-reconfigurable micromachines. The combination of a versatile biopolymer material format, favorable mechanical softness, and programmable shape-morphing, offers directions for advanced biotic/abiotic interfaces. The ease of functionalization of silk hydrogels, together with the facile implementation of on-demand 3D deformation to enable "personalized" conformal contact with tissue architectures, suggests paths for multifunctional and self-adaptive biointegrated devices for biomedical applications, including tissue regeneration, artificial organs, cardiac pacemakers, neutral stimulation and recording, and drug delivery systems. The feasibility of integrating silk hydrogels with flexible electrodes (e.g., CNTs, conductive hydrogels) supports the generation of soft actuators with dynamic, reversible, and tunable actuation in response to electrical stimuli, further expanding the utility of this silk material system as a bridge between soft robotic technologies and biomedical applications. The addition of 3D shape programming to silk material technology suggests avenues for future designs of various intelligent, 3D optical, electrical, magnetic, and thermal devices based on silk materials.

Materials and Methods

SF Solution Preparation. The SF solution was prepared following a well-established procedure reported previously (51). Briefly, *B. mori* silkworm cocoons were boiled in a 0.02 M Na_2CO_3 solution for 30 min and then rinsed with distilled water to remove the sericin layer. After dying for 2 d, the remaining silk fiber was dissolved in a 9.3 mol/L LiBr solution at 60 °C for 4 h, and then dialyzed against distilled water for 72 h to completely remove LiBr. Finally, SF solution with a concentration of about 6 wt% was obtained after further centrifugation and purification.

Fabrication of Homogeneous and Gradient Hydrogels. HRP, type VI lyophilized powder was mixed with deionized water to form a 40 mg mL^{-1} stock solution with a concentration of 10,000 U mL^{-1}. The HRP stock solution was added to the 6 wt% silk solution in a ratio of 12 Units of HRP to 1 mL silk solution. To prepare homogeneous hydrogels (SF-H-gel), 0.1 wt% H_2O_2 solution was added to the silk/HRP solution, for a final concentration of 0.3, 1, 2, and 4 mM, and mixed by gentle shaking to initiate the cross-linking reaction. The reaction mixture was incubated overnight at room temperature in air until complete gelation. To prepare gradient hydrogels (SF-G-gel), the prepared precursor solution was

injected into a PDMS mold, which was sandwiched between two pieces of ITO glass (6 ohm) that work as the positive and negative electrodes. After the complete gelation, a direct current electric field with a voltage of 1 V mm^{-1} was applied to induce the migration of protein network structure toward the anode side to form the gradient hydrogel.

Fabrication of Shape-Morphing Hydrogels. Silk hydrogels formed with 4 mM H_2O_2 were used to prepared shape-morphing hydrogels. After releasing the gradient hydrogel from the electrodes, the gel bent up suddenly toward the anode (high cross-link density region) due to the anisotropic distribution of protein network structure (cross-link density). PDMS molds with designed patterns created by a commercial CO_2 laser cutter (Speedy100R, Trotec Laser, Austria) were utilized to prepare shape-morphable hydrogels of different geometries. For Kirigami pattern preparation, as-prepared silk homogeneous hydrogels were directly used for laser cutting process (48). The laser power intensity was 25% of the maximum energy, and the speed was fixed at 1 step s^{-1} for a 5-mm-thick hydrogel. For the recovery experiments, the deformed hydrogels were equilibrated in distilled water at room temperature for 12 h. In cases where reversibility of the shape was not desired (e.g., fixation of shape), the morphing hydrogel was immersed into EtOH for different times.

Preparation of CNT Sheets and Hydrogel/CNT Bilayer Structure. Aligned CNT arrays were synthesized by chemical vapor deposition according to a previous report (52). The iron (1.5 nm) and Al_2O_3 (5 nm) were deposited on a silicon substrate as the catalyst by using an e-beam evaporator (DZS-500, Shenyang Keyi, China). The C_2H_2 with a flow rate of 90 sccm was used as the carbon source, and a mixture of Ar and H_2 was used as the carrier gas. Growth lasted for 10 min at 740 °C. The 15 layers of CNT sheets were drawn out from the CNT array and transferred to a thin polytetrafluoroethylene plate. To prepare the SF-H-gel/CNT bilayer system, a PDMS mold (4 cm × 0.5 cm × 0.1 cm) was carefully placed on the CNT sheets, followed by the injection of a precursor solution of silk hydrogel for gelation. The prepared bilayer structure was easily peeled off from the polytetrafluoroethylene plate. To induce shape transformation, an electric field was applied to the bilayer system by using the CNT layer and an ITO glass as the positive and negative electrodes, respectively.

MD Simulation. The constructed protein amino acid sequence to represent the SF was as follows:

GAGAGSGAASGAGAGYSGFGPYVANGGYSGYEYAWSSESDFGAGAGSGAASG AGAGYSGFGPYVANGGYSGYEYAWSSESDFGAGAGSGAASGAGAGYSGFGPYVANGG YSGYEYAWSSESDFGAGAGSGAASGAGAGYSGFGPYVANGGYSGYEYAWSSESDFGA GAGSGAASGAGAGYSGFGPYVANGGYSGYEYAWSSESDFGAGAGSGAASGAGAG YSGFGPYVANGGYSGYEYAWSSESDFGAGAGSGAASGAGAGYSGFGPYVANGGYSGY EYAWSSESDFGAGAGSGAASGAGAGYSGFGPYVANGGYSGYEYAWSSESDFGAG AGSGAASGAGAGYSGFGPYVANGGYSGYEYAWSSESDFGAGAGSGAASGAGAGYS GFGPYVANGGYSGYEYAWSSESDFGAGAGSGAASGAGAGYSGFGPYVANGGYSG YEYAWSSESDFGAGAGSGAASGAGAGY.

The long chain-like structure of the silk protein was generated by the tleap module of the amber program (53). The ab-initio structure prediction was performed using MD under a generalized born implicit solvent model. The Nanoscale Molecular Dynamics 2.14 program package was used for MD simulations (54). The cutoff distance for the calculation of the Born radius was set to 12 Å, and the ion concentration was set to 0.05 M. The structure and force field parameters of the silk proteins were described by using the CHARMM36m force field parameter set (55). The simulation temperature was set to 25 °C and controlled by a Langevin thermostat (56). All bond lengths containing hydrogen atoms were constrained by the SHAKE algorithm. The integration step was 2 fs. The silk protein was first subjected to 50,000 steps of conjugation gradient minimization to release the high-energy contact region. Thereafter, MD simulations of 400 ns were performed to obtain stable silk-protein structures. The above ab-initio predicted structure also required further structural optimization under an explicit solvent. The water molecules were adopted by using the model of transferable intermolecular potential with 3 points. In order to be consistent with the protein concentration used in the experiment, the minimum distance from the solute to the solvent box boundary was set to 22.4 Å. A certain number of sodium ions was added to the water to keep the electrical neutrality of the system. The final size of the simulated system was 100.5 × 98.9 × 126.6 $Å^3$. The short-range nonbonded interaction cutoff distance was set to 12 Å, and the nonbonded interaction list distance was set to 14 Å during the MD simulation. The integration step was 1 fs. The simulation temperature was 25 °C, and the system temperature was controlled using a Langevin thermostat. The system pressure was set to 1 atm, and the pressure control was based on the modified Nosé-Hoover Langevin piston method (57). The simulation system, with the protein backbone atoms constrained at a force constant of 50 kcal mol^{-1} $Å^{-2}$, was energy minimized by 50,000 steps of the conjugation gradient. After that, the NVT simulation was performed for 1 ns. Pressure control was turned on, and 1-ns NPT simulations were performed. Thereafter, the constraint potential energy was gradually and uniformly reduced to 0 over 2 ns of simulation time, and finally, the whole system was subjected to 6 ns of conventional MD simulations under unrestricted conditions. The resulting final structure was used as the starting structure for the simulations under electric field conditions. The setup of the MD simulation under electric field conditions was almost the same as before, except that all the simulation time steps were 2 fs, while all bonds containing hydrogen atoms were constrained by the SHAKE algorithm. The direction of the applied electric field followed the Z-axis direction, and the final simulation trajectories were used for the motion analysis of the silk protein. A total of four field strength values were chosen for the MD simulations under electric field conditions, including three field strengths that were along the positive Z-axis direction (1 mV/Å, 5 mV/Å, 10 mV/Å), and one 5 mV/Å field strength aligned with the negative Z-axis direction. All the representative snapshots for protein movement were produced using visualized MD Molecular Graphics Viewer.

Structural and Properties Characterization. Field emission SEM (S-8100, Hitachi, Japan) was used to analyze the cross-sectional morphology of the gradient hydrogels. The 3D microstructures of the gradient hydrogels were analyzed using a high-resolution X-ray 3D microscope (nanoVoxel 2000, Sanying, China) by transmitting X-ray through the sample with a rotation step of 0.33° and an exposure time of 1.70 s, and scanning 360° around the object. Images were acquired with a scaled pixel size of 1.86 μm. Rheological and compression measurements were conducted on the hydrogels to determine their mechanical properties. All rheology was performed using an HR 20 rheometer (TA Instruments, USA) with a stainless-steel parallel plate of 25 mm in diameter at 25 °C. A dynamic time sweep was performed at 1 Hz with a 1% applied strain for 600 s to determine the stability of the hydrogels. Dynamic frequency (0.1 to 100 rad/s at 1% strain) and amplitude sweeps (0.1% - to failure, at 1 Hz) were conducted to analyze elastic behavior of resulting hydrogels (n = 3). The compression tests were performed using a universal testing machine (HY0850, Heng Yi, China) at 25 °C and 45% relative humidity. The cylindrical silk hydrogel with 10 mm in diameter and 5 mm in initial thickness was compressed to a strain of 50% at a loading rate of 1 mm/min. For cyclic compression tests, the sample was loaded to a strain of 45% and immediately unloaded to zero strain then reloaded until 50 cycles. The tensile tests of the silk hydrogels at room temperature were performed on an Instron 5,565 at a strain rate of 10 mm min^{-1}. The hydrogel sheet was cut into dumbbell-shaped samples, with a gauge length of 20 mm and a width of 1 mm. FTIR was conducted to investigate the structural conformations of the hydrogels. All FTIR was carried out on a Nicolet FTIR IS50 spectrometer (Thermo Scientific, USA) equipped with a horizontal MIRacle ATR attachment. All FTIR spectra were collected in the wavenumber range of 4,000 to 600 cm^{-1}at 4 cm^{-1} resolution with an average of 96 scans. A fiber-optic spectrometer (PG2000-PRO-EX, IdeaOptics, China) was used to evaluate the transmissivity of the hydrogels. The transmittance at wavelength of 600 nm was calculated for comparison. The deformation and curvature changes of morphing hydrogels were recorded by a digital camera (850D, Canon, Japan) and analyzed with Image J.

FEA. To explore the shape morphing mechanism, all simulation in this work was carried out with the commercially available software COMSOL Multiphysics 5.4. The FEA is based on the assumptive model of SF-H-gel with a linear distribution of protein chains for simplification. Correspondingly, a local volumetric change associated with the mass changes of the polymer chains follows a similar linear relation. Parameters of the actual size and experimentally obtained Young's moduli SF-H-gel were adopted for simulation. The built-in *Solid Mechanics Modulus* was utilized to solve quasistatic mechanical equilibrium for finite solid deformation. The prescribed volumetric swelling was implemented by taking advantage

of the analogy with *Thermal Expansion*, and the Neo-Hookean material model defined the constitutive behavior of SF-H-gel.

Ex Vivo Attachment Experiments. All rabbit tissues and organs used for ex vivo attachment experiments were kindly donated from the First Medical Center, Chinese People's Liberation Army General Hospital, the animal work was approved by the Ethical Committee of Laboratory Animals of Chinese People's Liberation Army General Hospital (No. S2021-226-01).

Cytotoxicity, Biocompatibility, and Biodegradation. The cytotoxicity of the gradient hydrogel was assessed by using a cell count kit (CCK-8) and stained with Live/Dead kit. Briefly, mouse BMSCs were seeded into 96-well plates at a density of 5×10^3 cells/well and incubated in an incubator (37 °C, 5% CO_2). All gradient hydrogel samples were sterilized by exposing to ultraviolet (UV) light for 1 h. After placing the sample into 24-well plate, BMSCs were seeded and maintained on the gradient hydrogel at a density of 5,000 cells per well, and incubated in an incubator (37 °C, 5% CO_2) for 24 h. After the incubation, 10 μL of CCK-8 was added into each well, followed by incubation for another 2 h at 37 °C. Growth medium without the samples was used as a control. The cell viability was measured at wavelength of 450 nm by using the multifunctional microplate reader (EnSpire, PerkinElmer, USA). The assay was performed in five replicate wells, and three parallel experiments for each sample were conducted. For the Live/Dead test, BMSCs were seeded and maintained on the SF-G-gel at a density of 250,000 cells per well, and incubated in an incubator (37 °C, 5% CO_2) for 24 h. BMSCs were stained with Live/Dead kit for 15 min in the dark and observed by an Olympus TH4-200 fluorescence microscope (Olympus Corporation, Japan). The gradient hydrogels were prepared in an aseptic manner and were sterilized by ETO and UV treatment. Eight-week-old Kunming mice were anesthetized with isoflurane (1 to 3% in oxygen) in an anesthetizing chamber and maintained by using a nose cone. The back hair of the mice was shaved, and the subcutaneous space was exposed by skin incision and dissection surgery, followed with the hydrogel sample implantation in the subcutaneous area. After the 14 d of implantation, the mice were killed by CO_2 inhalation. The subcutaneous tissues were excised and fixed in 10% formalin for hematoxylin and eosin (H&E) staining and histological analyses. The protein expressions (α-SMA, CD68, COL-I) were analyzed by immunofluorescence staining. In brief, the hydrogel samples (n = 5 per group) were implanted into the subcutaneous space of the mice as described above, and the subcutaneous tissues were sectioned at 14 d of implantation. Then the slides were fixed with 4% paraformaldehyde, followed by immunostaining at Wuhan Servicebio Technology Co., Ltd. The fluorescence intensity of expressed antibodies was analyzed by CaseViewer software. To evaluate the degradation behavior of SF-G-gel and SF-H-gel, each hydrogel specimen was punched into a cylindrical shape and subjected to incubation at 37 °C in PBS solution, 0.01 and 1 U mL^{-1} protease XIV (type XIV from *Streptomyces griseus*, Sigma-Aldrich) PBS solution, respectively. Each hydrogel sample was exposed to 2 mL of the respective incubation solution. Following the removal of the enzyme solution, the hydrogels were thoroughly rinsed in distilled water, subjected to lyophilization, and weighed. The degradation results are presented as the mass fraction of the initial weight at day 0 (n = 3 per processing condition).

Electrical Property Measurements of the Hydrogel/CNT Bilayer. To characterize the electrical properties of the hydrogel/CNT bilayer, silver paste was applied on the two ends of the CNT sheets to ensure a stable connection between the CNT sheets. The thickness of the 15 layers CNT array was confirmed by using the SEM. The electrochemical impedance of the hydrogel/CNT was evaluated by placing the samples on a conductive ITO glass with the CNT-coated side upward. Alternating voltage (10 mv), ranging from 0.1 Hz to 100,000 Hz, was applied to the sample by an electrochemical workstation. The measurement of CIC of the hydrogel/CNT was conducted by using a three-electrode method in the PBS solution. The CNT layer was used as the working electrode, while Pt foil and Ag/AgCl (saturated in KCl aqueous solution) were used as counter electrode and reference electrode, respectively. Biphasic pulses of ± 0.5 V with a period of 20 ms (total 400 ms) were applied by using an electrochemical workstation (CS310X, Corrtest, China). The output voltage and current were recorded to analyze the CIC values.

In Vivo Sciatic Nerve Stimulation. All animal experiments were approved by the Ethical Committee of Laboratory Animals of Nantong University (No. S20210302-047), and all the procedures were conducted following the guidelines of the Care and Use of Laboratory Animals. The prepared SF-G-gel/CNT bilayer strip (40 mm in length and 1 mm in width) connected to a copper wire by silver conductive paste was used as the electrode for neural stimulation. All the hydrogel/CNT electrodes were prepared in an aseptic manner. For sciatic nerve stimulation, the New Zealand rabbit was anesthetized by ear vein injection of chloral hydrate (5 mg/kg). After shaving, a skin incision of 10 cm in length was created to dissect the gluteal muscle near the hip to expose the sciatic nerve. A pair of SF-G-gel/CNT electrodes were twined on the exposed sciatic nerve, with one electrode being rolled onto the proximal end of the sciatic nerve (near the spinal cord) to connect to the function generator and the other electrode being winded onto the distal end of the sciatic nerve, which linked to the oscilloscope probe. The grounding electrode was clamped to the skin near the incision. Biphasic pulses with 1 Hz generated by a function generator (UPO2104CS, UNI-T, China) was used for sciatic nerve stimulation, and the oscilloscope was used to receive and record the signal transmitted through the conductive electrode–sciatic nerve system. The angle changes of the feet were analyzed by ImageJ.

Statistical Analysis. Data are shown as mean ± SDs. Differences between two groups were analyzed by Student's *t* test. One-way ANOVA followed by Tukey's multiple comparison test was used to assess the differences between multiple samples. The significance thresholds were $^*P \leq 0.05$ for both *t* test and ANOVA. NS indicates no statistically significant differences.

Data, Materials, and Software Availability. The data that support the findings of this study are available within the paper and its supporting information.

ACKNOWLEDGMENTS. This work was supported by the National Key Research and Development Program of China (No.2021YFA1202000), the National Natural Science Foundation of China (No. 62175102, No. 52103084), the Natural Science Foundation of Jiangsu Province, Major Project (No. BK20212004), the Program for Innovative Talents and Entrepreneurs in Jiangsu (No. JSSCTD202138), and the Start-up Fund at the Nanjing University (No. 14912226).

Author affiliations: [a]National Laboratory of Solid State Microstructures, Key Laboratory of Intelligent Optical Sensing and Manipulation, College of Engineering and Applied Sciences, and Collaborative Innovation Center of Advanced Microstructures, Nanjing University, Nanjing 210023, China; [b]Department of Biomedical Engineering, Tufts University, Medford, MA 02155; and [c]Key Laboratory of Neuroregeneration, Collaborative Innovation Center of Neuroregeneration, Nantong University, Nantong 226001, China

Author contributions: Yushu Wang and Yu Wang designed research; Yushu Wang, L.L., Y.-E.J., T.W., Y.F., X.L., G.L., T.Z., L.W., and Q.H. performed research; Yushu Wang, L.L., Y.-E.J., Y.Z., and Yu Wang analyzed data; and Yushu Wang, Yu Wang, D.L.K., and Y.L. wrote the paper.

1. Y. Forterre, J. M. Skotheim, J. Dumais, L. Mahadevan, How the Venus flytrap snaps. *Nature* **433**, 421–425 (2005).
2. S. Armon, E. Efrati, R. Kupferman, E. Sharon, Geometry and mechanics in the opening of chiral seed pods. *Science* **333**, 1726–1730 (2011).
3. J. C. Nawroth *et al.*, A tissue-engineered jellyfish with biomimetic propulsion. *Nat. Biotechnol.* **30**, 792–797 (2012).
4. D. Rus, M. T. Tolley, Design, fabrication and control of soft robots. *Nature* **521**, 467–475 (2015).
5. S. Palagi, P. Fischer, Bioinspired microrobots. *Nat. Rev. Mater.* **3**, 113–124 (2018).
6. J. M. Taylor *et al.*, Biomimetic and biologically compliant soft architectures via 3D and 4D assembly methods: A perspective. *Adv. Mater.* **34**, 2108391 (2022).
7. D. Shah *et al.*, Shape changing robots: Bioinspiration, simulation, and physical realization. *Adv. Mater.* **33**, 2002882 (2021).
8. T. H. Ware, M. E. McConney, J. J. Wie, V. P. Tondiglia, T. J. White, Voxelated liquid crystal elastomers. *Science* **347**, 982–984 (2015).
9. T. J. White, D. J. Broer, Programmable and adaptive mechanics with liquid crystal polymer networks and elastomers. *Nat. Mater.* **14**, 1087–1098 (2015).
10. Y. Zhao *et al.*, Twisting for soft intelligent autonomous robot in unstructured environments. *Proc. Natl. Acad. Sci. U.S.A.* **119**, e2200265119 (2022).
11. J. Kim, J. A. Hanna, M. Byun, C. D. Santangelo, R. C. Hayward, Designing responsive buckled surfaces by halftone gel lithography. *Science* **335**, 1201–1205 (2012).
12. K. K. Liu *et al.*, Programmable reversible shape transformation of hydrogels based on transient structural anisotropy. *Adv. Mater.* **32**, 2001693 (2020).
13. C. N. Zhu *et al.*, Reconstructable gradient structures and reprogrammable 3D deformations of hydrogels with coumarin units as the photolabile crosslinks. *Adv. Mater.* **33**, 2008057 (2021).
14. A. Nojoomi, J. Jeon, K. Yum, 2D material programming for 3D shaping. *Nat. Commun.* **12**, 603 (2021).
15. E. Siefert, E. Reyssat, J. Bico, B. Roman, Bio-inspired pneumatic shape-morphing elastomers. *Nat. Mater.* **18**, 24–28 (2019).

16. Y. Zhang *et al.*, Climbing-inspired twining electrodes using shape memory for peripheral nerve stimulation and recording. *Sci. Adv.* **5**, eaaw1066 (2019).
17. W. J. Peng, G. G. Zhang, Q. Zhao, T. Xie, Autonomous off-equilibrium morphing pathways of a supramolecular shape-memory polymer. *Adv. Mater.* **33**, 2102473 (2021).
18. S. J. Jeon, A. W. Hauser, R. C. Hayward, Shape-morphing materials from stimuli-responsive hydrogel hybrids. *Acc. Chem. Res.* **50**, 161–169 (2017).
19. X. J. Liu *et al.*, Recent advances in stimuli-responsive shape-morphing hydrogels. *Adv. Funct. Mater.* **32**, 2203323 (2022).
20. X. Y. Liu, J. Liu, S. T. Lin, X. H. Zhao, Hydrogel machines. *Mater. Today* **36**, 102–124 (2020).
21. H. Yuk, J. J. Wu, X. H. Zhao, Hydrogel interfaces for merging humans and machines. *Nat. Rev. Mater.* **7**, 935–952 (2022).
22. M. Cianchetti, C. Laschi, A. Menciassi, P. Dario, Biomedical applications of soft robotics. *Nat. Rev. Mater.* **3**, 143–153 (2018).
23. E. Palleau, D. Morales, M. D. Dickey, O. D. Velev, Reversible patterning and actuation of hydrogels by electrically assisted ionoprinting. *Nat. Commun.* **4**, 2257 (2013).
24. A. S. Gladman, E. A. Matsumoto, R. G. Nuzzo, L. Mahadevan, J. A. Lewis, Biomimetic 4D printing. *Nat. Mater.* **15**, 413–418 (2016).
25. J. D. Tang, Q. F. Yin, Y. C. Qiao, T. J. Wang, Shape morphing of hydrogels in alternating magnetic field. *ACS Appl. Mater. Inter.* **11**, 21194–21200 (2019).
26. Q. L. Zhu *et al.*, Light-steered locomotion of muscle-like hydrogel by self-coordinated shape change and friction modulation. *Nat. Commun.* **11**, 5166 (2020).
27. H. Zhao *et al.*, Biomimetic 4D-printed breathing hydrogel actuators by nanothylakoid and thermoresponsive polymer networks. *Adv. Funct. Mater.* **31**, 2105544 (2021).
28. Z. Zhao *et al.*, Digital printing of shape-morphing natural materials. *Proc. Natl. Acad. Sci. U.S.A.* **118**, e2113715118 (2021).
29. Z. Q. Zheng *et al.*, Programmable aniso-electrodeposited modular hydrogel microrobots. *Sci. Adv.* **8**, eade6135 (2022).
30. J. M. Viola *et al.*, Guiding cell network assembly using shape-morphing hydrogels. *Adv. Mater.* **32**, 2002195 (2020).
31. Z. W. Li, N. V. Myung, Y. D. Yin, Light-powered soft steam engines for self-adaptive oscillation and biomimetic swimming. *Sci. Robot.* **6**, eabi4523 (2021).
32. X. S. Qian *et al.*, Artificial phototropism for omnidirectional tracking and harvesting of light. *Nat. Nanotechnol.* **14**, 1048–1055 (2019).
33. H. Haider *et al.*, Exceptionally tough and notch-insensitive magnetic hydrogels. *Soft Matter* **11**, 8253–8261 (2015).
34. Q. Shi *et al.*, Bioactuators based on stimulus-responsive hydrogels and their emerging biomedical applications. *NPG Asia Mater.* **11**, 64 (2019).
35. Y. B. Lee *et al.*, Induction of four-dimensional spatiotemporal geometric transformations in high cell density tissues via shape-changing hydrogels. *Adv. Funct. Mater.* **31**, 2010104 (2021).
36. Z. H. Zhang, Y. Wang, Q. Wang, L. R. Shang, Smart film actuators for biomedical applications. *Small* **18**, 2105116 (2022).
37. F. G. Omenetto, D. L. Kaplan, New opportunities for an ancient material. *Science* **329**, 528–531 (2010).
38. C. Li *et al.*, Design of biodegradable, implantable devices towards clinical translation. *Nat. Rev. Mater.* **5**, 61–81 (2020).
39. T. Venkatesan, S. Williams, Brain inspired electronics. *Appl. Phys. Rev.* **9**, 010401 (2022).
40. C. Ye *et al.*, Self-(Un)rolling biopolymer microstructures: Rings, tubules, and helical tubules from the same material. *Angew. Chem. Int. Ed.* **127**, 8610–8613 (2015).
41. R. Ma *et al.*, Pop-up conducting large-area biographene kirigami. *ACS Nano* **12**, 9714–9720 (2018).
42. B. P. Partlow *et al.*, Highly tunable elastomeric silk biomaterials. *Adv. Funct. Mater.* **24**, 4615–4624 (2014).
43. G. G. Leisk, T. J. Lo, T. Yucel, Q. Lu, D. L. Kaplan, Electrogelation for protein adhesives. *Adv. Mater.* **22**, 711–715 (2010).
44. T. Yucel, N. Kojic, G. G. Leisk, T. J. Lo, D. L. Kaplan, Non-equilibrium silk fibroin adhesives. *J. Struct. Biol.* **170**, 406–412 (2010).
45. N. Kojic *et al.*, Ion electrodiffusion governs silk electrogelation. *Soft Matter* **8**, 2897–2905 (2012).
46. J. E. Bressner *et al.*, Rapid fabrication of silk films with controlled architectures via electrogelation. *J. Mater. Chem. B* **2**, 4983–4987 (2014).
47. Q. Lu *et al.*, Hydrogel assembly with hierarchical alignment by balancing electrostatic forces. *Adv. Mater. Interfaces* **3**, 1500687 (2016).
48. Y. H. Zhang *et al.*, A mechanically driven form of Kirigami as a route to 3D mesostructures in micro/nanomembranes. *Proc. Natl. Acad. Sci. U.S.A.* **112**, 11757–11764 (2015).
49. J. Deng *et al.*, Electrical bioadhesive interface for bioelectronics. *Nat. Mater.* **20**, 229–236 (2021).
50. G. Li *et al.*, Highly conducting and stretchable double-network hydrogel for soft bioelectronics. *Adv. Mater.* **34**, e2200261 (2022).
51. D. N. Rockwood *et al.*, Materials fabrication from Bombyx mori silk fibroin. *Nat. Protoc.* **6**, 1612–1631 (2011).
52. L. Ye *et al.*, Stabilizing lithium into cross-stacked nanotube sheets with an ultra-high specific capacity for lithium oxygen batteries. *Angew. Chem. Int. Ed.* **58**, 2437–2442 (2019).
53. Y. Duan *et al.*, A point-charge force field for molecular mechanics simulations of proteins based on condensed-phase quantum mechanical calculations. *J. Comput. Chem.* **24**, 1999–2012 (2003).
54. J. C. Phillips *et al.*, Scalable molecular dynamics on CPU and GPU architectures with NAMD. *J. Chem. Phys.* **153**, 044130 (2020).
55. J. Huang *et al.*, CHARMM36m: An improved force field for folded and intrinsically disordered proteins. *Nat. Methods* **14**, 71–73 (2017).
56. D. Quigley, M. I. J. Probert, Langevin dynamics in constant pressure extended systems. *J. Chem. Phys.* **120**, 11432–11441 (2004).
57. S. E. Feller, Y. H. Zhang, R. W. Pastor, B. R. Brooks, Constant-pressure molecular-dynamics simulation–The Langevin piston method. *J. Chem. Phys.* **103**, 4613–4621 (1995).